Research & Reviews: Journal of
Space Science & Technology

https://journals.stmjournals.com/rrjosst

ISSN: 2321-2837 (Online)
ISSN: 2321-6506 (Print)
Volume 14, Issue 1, 2025
January–April
DOI (Journal): 10.37591/RRJoSST

Research RRJoSST

Influence of Photoelectrons on Spacecraft Charging for Artificial Orbiting Spacecraft

Rizwan H. Alad[1,*], Vidhi Mistry[2], Hetvi Makwana[2], Keyurkumar Patel[1], Ashish Pandya[1]

Abstract

For the purpose of evaluating the temporal body potential and capacitance of an artificial orbiting spacecraft, this research analyzes the impact of photoelectrons on spacecraft charging. A metallic rectangular cuboid and two coplanar metallic rectangular plates compose the spacecraft model. The Runge-Kutta method is used to calculate the body potential, and the method of moments is used to calculate the capacitance. Depending on the spacecraft's inclination angle, solar energy from the Sun is directly impacted on the area that receives sunlight. The study also explores how an excessive buildup of charge can cause operational challenges, such as electrical discharges, disruptions in communication, and potential harm to delicate electronic systems. This study explores how spacecraft accumulate charge in space and the role of photoelectrons in this process. It suggests improved methods for managing charges, including the use of specialized materials and protective coatings to minimize potential risks. The findings support the development of more robust spacecraft designed for extended missions. Depending on the spacecraft material's photon efficiency, the incident solar radiation ejects photoelectrons from the spacecraft surface, increasing the spacecraft body's positive charge. In addition to accounting for different wavelengths, the variation in body potential is established both with and without the photoelectric effect. It is discovered that the variance of body potential is significantly influenced by the photoelectric current. For different scenarios, the spacecraft's body potential's temporal behavior is examined.

Keywords: Spacecraft charging, method of moments (MoM), Runge-Kutta method, photoelectric effect, body potential

INTRODUCTION

Electromagnetic radiation from the sun has an important part in spacecraft charging. Before being launched, materials for space applications are thoroughly explained in the lab; however, once in orbit, they are subjected to the extreme conditions of space, which significantly change their properties [1, 2]. One of the biggest threats to the integrity of satellites and subsystems is flashover and arcing caused by surface charging, which is brought on by thermal plasma with energy up to about 100 keV [3]. Thanks to several software programs, such as the open-source European SPIS software [4] or its North American or Japanese equivalents [5, 6], it is now possible to precisely recreate the charging process and simulate how the spacecraft interacts with the surrounding plasma. Spacecraft charging is significantly impacted by solar radiation from the sun [7]. Electrostatic discharge (ESD) is the result of variations in potential across the various surfaces of spacecraft caused by the unpredictable radiation [7–9]. Certain elements of spacecraft will remain in the shade even if they are working in the sun [10].

***Author for Correspondence**
Rizwan H. Alad
E-mail: rizwan_alad.ec@ddu.ac.in

[1]Professor, Department of Electronics & Communication Engineering, Faculty of Technology, Dharmsinh Desai University, Nadiad, Gujarat, India
[2]Student, Department of Electronics & Communication Engineering, Faculty of Technology, Dharmsinh Desai University, Nadiad, Gujarat, India

Received Date: February 14, 2025
Accepted Date: February 20, 2025
Published Date: March 03, 2025

Citation: Rizwan H. Alad, Vidhi Mistry, Hetvi Makwana, Keyurkumar Patel, Ashish Pandya. Influence of Photoelectrons on Spacecraft Charging for Artificial Orbiting Spacecraft. Research & Reviews: Journal of Space Science & Technology. 2025; 14(1): 36–46p.

Due to photoelectron emission, the potential of the day-side surface is usually a few volts positive relative to the ambient, but in the shadow, the hot electron flux from the ambient plasma can cause the potential to be hundreds to thousands of volts negative [11–20]. The intricate relationships between spaceship materials and their charging behavior in space have been further illuminated by recent studies. In their analysis of Van Allen Probe data, Sarno-Smith et al. [21] discovered a significant connection between spacecraft charging events and high electron pressures and electron energy flows, underscoring the significance of real-time monitoring to reduce hazards. In a similar vein, Dennison et al. (2023) examined threshold charging, highlighting the influence of electron emission properties of spacecraft materials [22] and showing how minor variations in the surrounding environment can result in sudden changes from small positive potentials to huge negative potentials. The requirement to take environmental electric fields into consideration when evaluating spacecraft charging was further supported by Wang et al. (2014), who investigated how variations in electric fields, such as plasma waves in Earth's magnetosphere, modulate emitted photoelectrons and cause possible variations [23].

The electrostatic discharge caused a system failure in the Anik-E1, E2, and geostationary satellites [23]. Secondary electrons, backscattered electrons, and photoelectrons are all taken into consideration when analyzing the net current density [23]. In certain space weather situations, photoelectron emission may not be sufficient to counterbalance the energetic ambient electrons, which normally drives the surface potential to positive for warm surfaces under quiet solar wind conditions [24]. The spacecraft will develop a negligible positive potential during the day-night interface as a portion of it will be in the sunlit region, where the photoelectron impact will be greater than the secondary electrons. On the other hand, photoelectrons do not have an effect in the sun-shadowed region, so the secondary electrons cause a very high negative impact [25]. The spacecraft body releases photoelectrons during the day, and the photoelectric current (I_{ph}) is affected by the wavelength of solar radiation, radiation intensity, effective area, and material photon efficiency. In order to simulate the spacecraft and its surface area, the study takes use of a model of a metallic rectangular cuboid with two coplanar rectangular plates connected to it. This work describes the effects of changes in the effective area on the body potential of the spacecraft over time in geostationary orbit, also known as geosynchronous equatorial orbit (GEO).

Using the method of moments (MoM), the capacitance and charge distribution of the structure can be determined using a metallic rectangular cuboid with two coplanar rectangular plates. This geometrical structure is divided into nonuniform rectangular subsections for analysis using MoM [26]. In order to generate the set of simultaneous equations, the unknown charge densities are extended using pulse functions as basic functions and delta functions as testing functions [27]. The unknown charge distribution (Q) on the surface of the spacecraft is calculated using the numerical method MoM. It is commonly known that the charge distribution varies very little in the center and mostly toward the conductor surface's borders [28].

In addition, the spacecraft's body potential (V) is calculated using the Runge-Kutta method, which makes it possible to determine its capacitance (C). The structure transforms into a metallic cuboid when the surface area of both coplanar plates becomes less than zero, and the resulting capacitance value roughly resembles the capacitance value stated in references [28] and [29]. It is discovered that the spacecraft's effective area affects the quantity of photoelectrons released, which causes an accumulation of positive charges on the body. The effects of various wavelengths on the spacecraft's body potential are further investigated in this research.

Without taking into consideration the photoelectric effect, it initially becomes apparent that the body potential is more negatively charged. Nevertheless, the body potential becomes less negatively charged when the photoelectric effect is considered. The body potential cannot become positive due to the presence of secondary and backscattered electrons. When the photoelectric effect is considered, the study emphasizes the important roles that the effective spacecraft area and photon efficiency of spacecraft material play. The duration- and wavelength-dependent changes in the spacecraft's body potential are demonstrated by simulations, considering the photoelectric effect and how it affects the hazard of ESD.

PROBLEM FORMULATION

The spacecraft charging mainly depends on plasma parameters, altitude of orbit and day-night interface in the spacecraft body. Depending upon the type of orbit, that is, low Earth orbit (LEO) or GEO, the spacecraft charged due to secondary electrons, backscattered electron, and photoelectron varies. The net current density (j_{net}) is given by

$$j_{net}=j_i+j_e+j_{ph}+j_{se} \tag{1}$$

where j_i and j_e are the current density of incident ion and electron, respectively, j_{ph} is the current density of photoelectrons, and j_{se} is the current density of secondary electron. When the net current density is zero, the spacecraft is considered to have zero potential with respect to plasma [25].

This study examines spacecraft geometry in GEO. Electrons that are released from a surface because of electromagnetic radiation, such as light or sunlight, are referred to as photoelectrons and are known as the photoelectric effect. Because these photoelectrons have a negative charge, they significantly contribute to the spacecraft's charging because, upon emission, the spacecraft's body potential gains a positive charge.

The photon efficiency of the spacecraft surface material determines how many electrons can be removed from the spacecraft body. Photon flux (ϕ) is now the number of photographs that incident on a plate each second. which is given by

$$\phi = \frac{P_r}{E} = \frac{P}{4\Pi r^2} \cdot \frac{A_e}{hf} = \frac{PA_e}{hf4\Pi r^2} \tag{2}$$

where h is Planck's constant of value 6.62607015 × 10^{-34} Joule-second, P_r is received power at spacecraft body on which solar radiation is referred as effective area A_e, E is the energy of photon at frequency f and P is the power of point source solar radiation. When frequency is above the threshold frequency and the photon efficiency of surface material also known as quantum efficiency (QE) is $\eta\%$, then the number of photoelectrons emitted per second (n) is given by

$$n = \frac{\phi . \eta}{100} \tag{3}$$

Substituting Equation (2) in Equation (3) we get,

$$n = \frac{PA_e\eta}{100 \times hf \times 4\pi r^2} \tag{4}$$

Now photoelectric current is given by

$$I_{ph} = ne$$

$$I_{ph} = \frac{PA_e\eta}{100 \times hf \times 4\pi r^2} \times e \tag{5}$$

where e is charge of electron with value 1.6 × 10^{-19} J. Value for intensity (I) of sunlight in GEO is equal to 1373.99 W/m^2, energy of photon is given by

$$E = \frac{hc}{\lambda} \tag{6}$$

where λ wavelength of solar radiation the intensity I at the distance r from source is given by

$$I = \frac{P}{4\Pi r^2} \tag{7}$$

Substituting Equations (6) and (7) in Equation (5),

$$I_{ph} = \frac{IA_e\eta}{100\times hc} \times e\lambda \tag{8}$$

The photoelectric current depends on the intensity of radiation (I), effective area (A_e) and photon efficiency of material (η). From the equation (8) we can find the value of photoelectric current of the spacecraft during photoelectric effect at daylight. Further the current density of photoelectrons is given by

$$J_{ph} = \frac{I_{ph}}{A} \tag{9}$$

where A is the total area of spacecraft.

This work proposes the spacecraft body to be a metallic rectangular cuboid with dimensions L, W, and H. As illustrated in Figure 1, the cuboid is attached to two coplanar rectangular plates with dimensions L1 W1 and L2 W2. The geometrical center point of the metallic cuboid is where the coordinate system's origin is located. The left side plate of the metallic cuboid is attached to Plate 1, which is W/2 distance from the origin and oriented parallel to the X–Y plane with the Z-axis perpendicular to the surface.

The potential at any arbitrary point due to charge distribution on the cuboid and rectangular plates [30] is given by

$$V = \frac{1}{4\pi\varepsilon_0}\int_s \frac{\rho(x',y',z')}{|r-r'|}\,ds \tag{10}$$

The surface 's' in Equation (10) is divided into three parts, one part is rectangular cuboid, and another two parts are rectangular plates. Thus Equation (10) can be written in the following form:

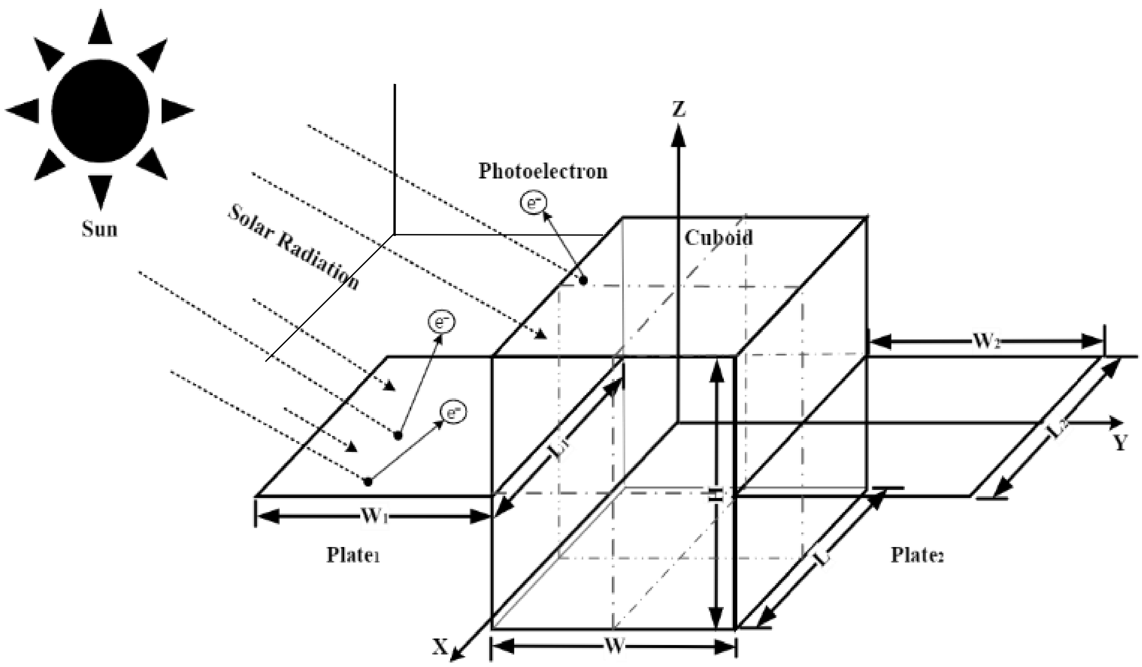

Figure 1. Photoelectric effect on metallic cuboid with two coplanar rectangular plates.

$$V = \frac{1}{4\pi\varepsilon_0}\left[\underbrace{\int_{s_1}\frac{\rho_1(x_1',y_1',z_1')}{|r-r_1'|}ds_1}_{V_1} + \underbrace{\int_{s_2}\frac{\rho_2(x_2',y_2',z_2')}{|r-r_2'|}ds_2}_{V_2} + \underbrace{\int_{s_3}\frac{\rho_3(x_3',y_3',z_3')}{|r-r_3'|}ds_3}_{V_3}\right] \tag{11}$$

where s_1, s_2 and s_3 represent the surfaces over the metallic cuboid, rectangular metallic plate_1 and plate_2 respectively.

The unknown charge densities over surfaces s_1, s_2, and s_3 are denoted by ρ_1, ρ_2, and ρ_3 in Equation (11). By solving the integral (11) with MoM, the capacitance of the structure as seen in Figure 1 can be calculated by determining the unknown charge distribution on the surfaces of the cuboid and the two coplanar plates. The surfaces of the building are separated into several nonuniform subsections in order to apply the MoM.

The unknown charge distributions appearing in the integral (10) is expressed in terms of known basis function as [31]

$$\rho_1(r') = \sum_{n=1}^{MN_a}\alpha_{an}f_n + \sum_{n=1}^{MN_b}\alpha_{bn}f_n + \cdots .. + \sum_{n=1}^{MN_f}\alpha_{fn}f_n$$
$$where\ \ \alpha_1 = \alpha_a + \alpha_b + \ldots + \alpha_f \tag{12}$$

$$\rho_2(r') = \sum_{n=MN_1+1}^{MN_2}\alpha_{2n}f_n \tag{13}$$

$$\rho_3(r') = \sum_{n=MN_1+MN_2}^{MN_3}\alpha_{3n}f_n \tag{14}$$

The basic functions *fn* are the pulse expansion functions given by

$$f_n = \begin{Bmatrix} 1, & r \in \Delta S_n \\ 0, & otherwise \end{Bmatrix} \tag{15}$$

Substituting (12), (13) & (14) in(11) and matching the boundary conditions for the potential at the center point of each subsection and following the procedure of references [32] and [33], the equations reduce to the form,

$$V_1 = \sum_{n=1}^{MN_1}\alpha_{1n}l_{11m1n} + \sum_{n=1+MN_1}^{MN_2}\alpha_{2n}l_{12m2n} + \sum_{n=1+MN_1+MN_2}^{MN_3}\alpha_{3n}l_{13m3n} \tag{16}$$

$$V_2 = \sum_{n=1}^{MN_1}\alpha_{1n}l_{21m1n} + \sum_{n=1+MN_1}^{MN_2}\alpha_{2n}l_{22m2n} + \sum_{n=1+MN_1+MN_2}^{MN_3}\alpha_{3n}l_{23m3n} \tag{17}$$

$$V_3 = \sum_{n=1}^{MN_1}\alpha_{1n}l_{31m1n} + \sum_{n=1+MN_1}^{MN_2}\alpha_{2n}l_{32m2n} + \sum_{n=1+MN_1+MN_2}^{MN_3}\alpha_{3n}l_{33m3n} \tag{18}$$

where $m_1 = 1,\ldots,MN_1$, $m_2 = 1,\ldots MN_2$ and $m_3 = 1,\ldots MN_3$.

The coefficient terms appearing in Equations (16) to (18) are of the form:

$$l_{11} = \int_{(n-1)\Delta x}^{n\Delta x} \int_{(n-1)\Delta y}^{n\Delta y} \frac{1}{\sqrt{(x-x')^2 + (y-y')^2}} dx'\,dy' \tag{19}$$

After carrying out the integration over variable *x'* in Equation (19), the following expression is obtained:

$$l_{11} = \int_{y_{n-1}}^{y_n} dy' \left[\log \frac{\sqrt{(x-x_{n-1})^2 + (y'_n - y)^2} + x - x_{n-1}}{\sqrt{(x-x_n)^2 + (y'_n - y)^2} + x - x_n} \right] \tag{20}$$

After carrying out the integration over variable *y'* in Equation (20) and matching the resulting expression at x_{m1} and y_{m1} respectively which are the midpoints of each sub-sections for *x* and *y*, the expression is obtained [31].

In this case, diagonal elements are not treated separately as the pulse function has been used as the basis function unlike that of references [30–34] where both basis as well as testing functions were used as delta functions. Similarly, the expressions for other co-efficient appeared in expressions (16) to (19) are obtained.

The set of simultaneous equations appearing in expressions (16) to (18) may be expressed in a matrix equation as under:

$$\begin{bmatrix} [l_{11m1n}] & [l_{12m2n}] & [l_{13m3n}] \\ [l_{21m1n}] & [l_{22m2n}] & [l_{23m3n}] \\ [l_{31m1n}] & [l_{32m2n}] & [l_{33m3n}] \end{bmatrix} \begin{bmatrix} [\alpha_{1n}] \\ [\alpha_{2n}] \\ [\alpha_{3n}] \end{bmatrix} = \begin{bmatrix} [V_1] \\ [V_2] \\ [V_3] \end{bmatrix} \tag{21}$$

The co-efficient matrix of (21) is of the order of $(MN_1+MN_2+MN_3)\times(MN_1+MN_2+MN_3)$ which is partitioned into nine square submatrices having each of the order $MN_1\times MN_1$, $MN_1\times MN_2$, $MN_1\times MN_3$, $MN_2\times MN_1$, $MN_2\times MN_2$, $MN_2\times MN_3$, $MN_3\times MN_1$, $MN_3\times MN_2$, $MN_3\times MN_3$, respectively. By using Equation (21), the unknown coefficients representing the charge density of each sub-section are obtained [31].

Total charge presented in the geometry of Figure 1 is

$$Q = Q_1 + Q_2 + Q_3 \tag{22}$$

Q_1, Q_2 and Q_3 are the total charge on the metallic rectangular cuboid, rectangular plate$_1$ and plate$_2$, respectively. These individual charges can be obtained from

$$Q_1 = \sum_{n=1}^{MN_1} \alpha_{1n} S_1(n) \tag{23}$$

$$Q_2 = \sum_{n=1}^{MN_2} \alpha_{2n} S_2(n) \tag{24}$$

$$Q_3 = \sum_{n=1}^{MN_3} \alpha_{3n} S_3(n) \tag{25}$$

where ΔS_1, ΔS_2 and ΔS_3 are the area of subsections in the metallic cuboid, rectangular plate$_1$ and plate$_2$, respectively.

The capacitance of the formation shown in Figure 1 is given as

$$C = \frac{Q}{V} \tag{26}$$

The variation of capacitance with the number of sub-sections of the structure shown in Fig. 1 and the converged value of the capacitance is 90.53 pF/m [31].

NUMERICAL RESULTS AND DISCUSSION

The orbit taken into consideration is GEO, where intensity I = 1373.99 W/m^2 at daylight, wavelength λ = 10–13 m, speed of light c = 3 × 108 m/s, Planck's constant h = 6.633 × 10-34 J.s, total area = 10 m^2, and photon efficiency is assumed η = 3%. The capacitance of the body is computed using the numerical technique. The MoM and body potential is computed using another numerical technique by Runge-Kutta.

Figure 2 shows the variation in voltage body potential with respect to time with 10% effective area of the total area. The curve represents the change in the body potential without the photoelectric effect, where the body potential reaches a steady-state value of –18779 V, and the above curve shows the change in body potential in consideration with the photoelectric effect, where the body potential reaches a steady-state value of –12939 V. The difference of 5840 V is observed; this means the body is getting positively charged by the photoelectric effect. When the number of solar photons is incident on the spacecraft body surface, the photoelectrons are emitted, and this number of photoelectrons is dependent on the effective area of the spacecraft (defined as the spacecraft surface area on which solar radiations are incident). The effective area (A_e) changes with respect to the inclination angle of the spacecraft body. As the effective area increases, the number of solar photons increases, which leads to a greater number of photoelectron emissions. As a result, the body gets positively charged.

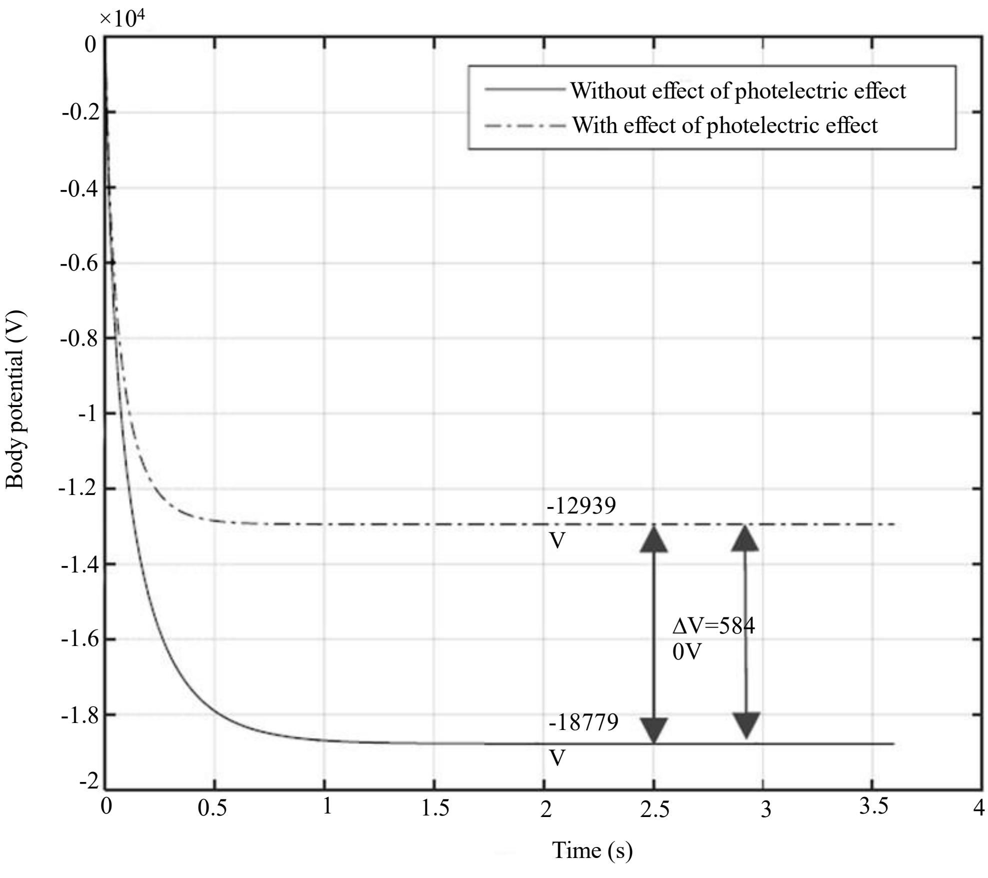

Figure 2. Variation in body potential with time.

Figures 3 and 4 show the variation in body potential with consideration of 20% and 30% effective area of spacecraft total area. Effective area with 20% of the total area reaches a steady state value of –9495.9 V and effective area with 30% of the total area reaches a steady-state value of –7083 V from 0.98 seconds. Figure 5 represents the curve of effective difference in body potential of spacecraft without the photoelectric effect and after the addition of the photoelectric effect, which is denoted as ΔV with varying the effective area of spacecraft by an increment of 10%. When the effective area increases, the body gets positively charged, so the difference in body potential also increases, and as a result, the plot gives a logarithmic curve.

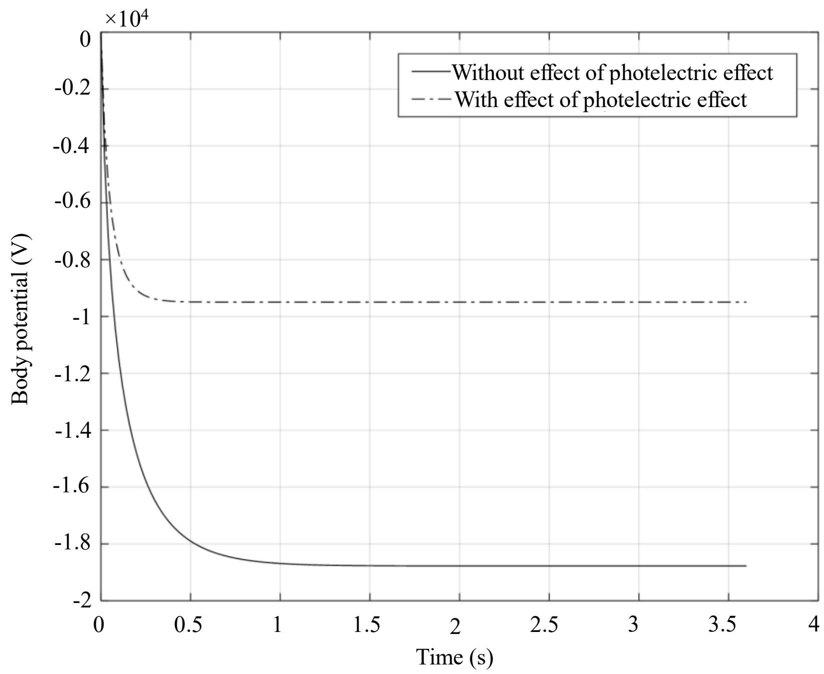

Figure 3. Variation in body potential with 20% effective area with time.

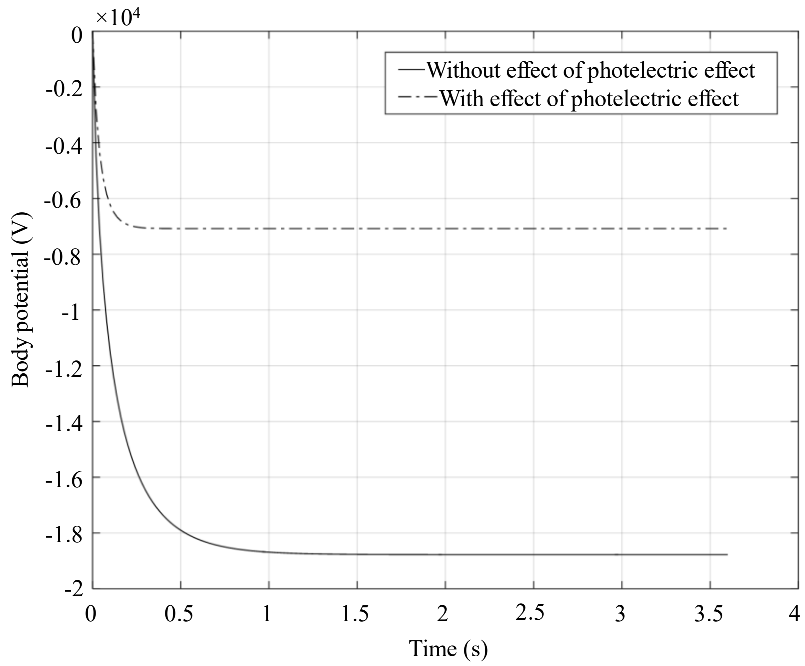

Figure 4. Variation in body potential with 30% effective area with time.

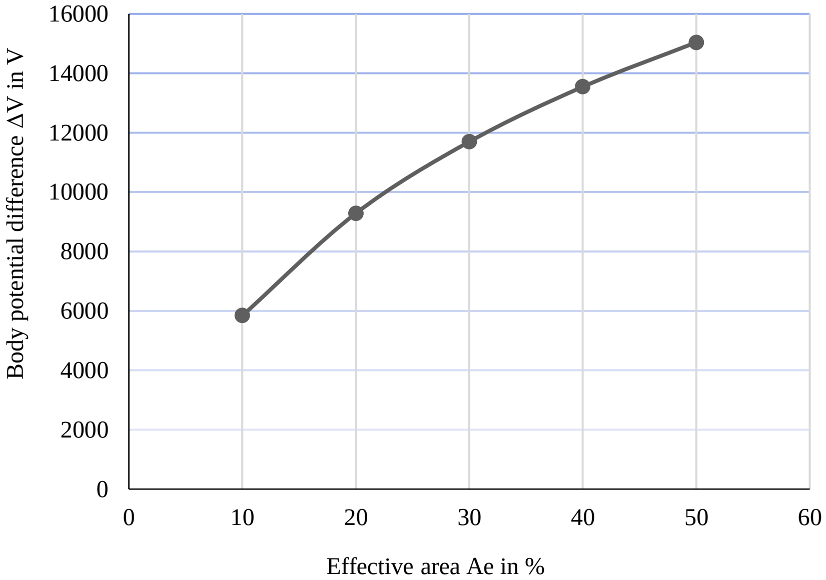

Figure 5. Variation in body potential difference with effective area.

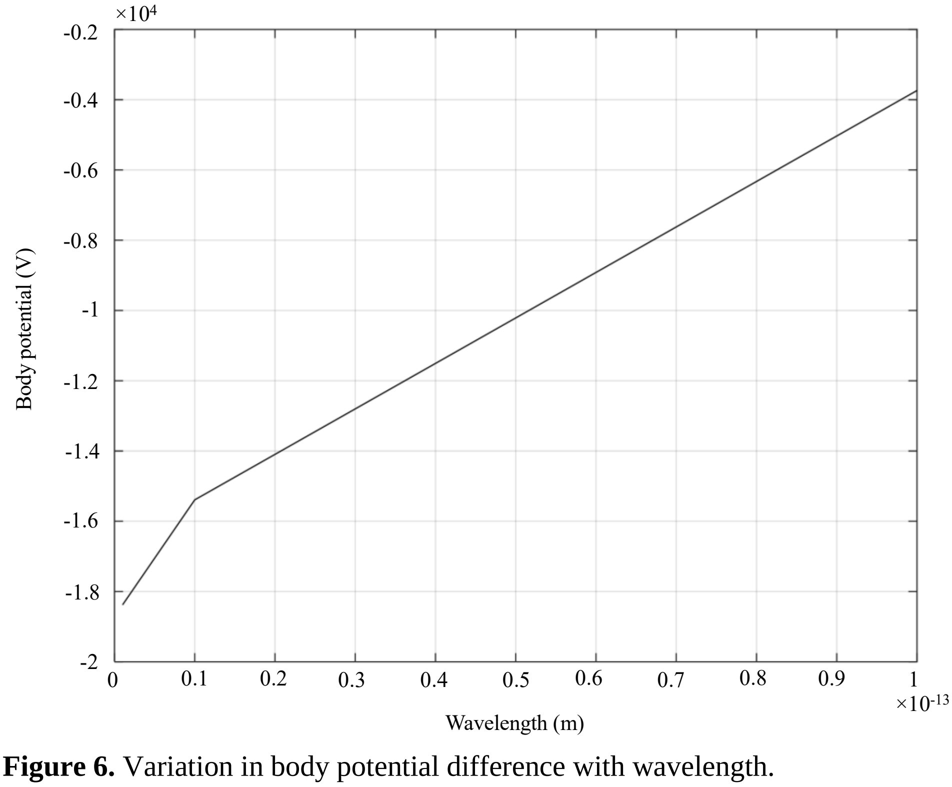

Figure 6. Variation in body potential difference with wavelength.

As shown in Figure 6, the decrement in wavelength leads the body potential to be more negative. Therefore, higher the value of wavelength, increases the body potential positively.

CONCLUSION

The capacitance of a structure having a metallic rectangular cuboid with two coplanar metallic rectangular plate is obtained by MoM with the value of 90.53 pF/m and the body potential is obtained using the Runge-Kutta method. This paper brings out quantitatively how the body potential is dependent on the effective area of the spacecraft, as depicted in Figure 5. The body potential of spacecraft with

50% effective area without photoelectric effect is –18779 V and with consideration of effect is –3728 V, so body potential difference become 15051 V. So, the spacecraft body becomes positively charged, and as the effective area increases, the body potential increases, and spacecraft body becomes more positively charged which leads to electrostatic discharge event. The body potential becomes less negatively charged with a decrease in the wavelength of solar radiation. The spacecraft body becoming positively charged leads to a greater difference in body potential, illustrated by a logarithmic curve as shown in Figure 5.

REFERENCES

1. Nakagawa T, Ishii T, Tsuruda K, Hayakawa H, Mukai T. Net current density of photoelectrons emitted from the surface of the GEOTAIL spacecraft. Earth Planets Space. 2000; 52: 283–292.
2. Kawasaki K, Inoue S, Ewang E, Toyoda K, Cho M. Measurement of electron emission yield by electrons and photons for space aged material. In: Proceedings of the 14th Spacecraft Charging Technology Conference, ESA/ESTEC, Noordwijk, Netherlands, April 4–8, 2016. pp. 1–7.
3. Koons HC. Summary of environmentally induced electrical discharges on the P78-2 (SCATHA) satellite. J Spacecraft Rockets. 1983; 20 (5): 425–431.
4. Matéo-Vélez JC, Theillaumas B, Sévoz M, Andersson B, Nilsson T, Sarrailh P, Thiébault B, Jeanty-Ruard B, Rodgers D, Balcon N, Payan D. Simulation and analysis of spacecraft charging using SPIS and NASCAP/GEO. IEEE Trans Plasma Sci. 2015; 43 (9): 2808–2816.
5. Mandell MJ, Davis VA, Cooke DL, Wheelock AT, Roth CJ. Nascap-2k spacecraft charging code overview. IEEE Trans Plasma Sci. 2006; 34 (5): 2084–2093.
6. Muranaka T, Hosoda S, Kim JH, Hatta S, Ikeda K, Hamanaga T, Cho M, Usui H, Ueda HO, Koga K, Goka T. Development of multi-utility spacecraft charging analysis tool (MUSCAT). IEEE Trans Plasma Sci. 2008; 36 (5): 2336–2349.
7. Garrett HB, Whittlesey AC. Spacecraft charging, an update. IEEE Trans Plasma Sci. 2000; 28 (6): 2017–2028.
8. Garrett HB, Whittlesey AC. Guide to Mitigating Spacecraft Charging Effects. Hoboken, NJ, USA: John Wiley & Sons; 2012.
9. Hastings D, Garrett H. Spacecraft-Environment Interactions. Cambridge, UK: Cambridge University Press; 2004.
10. Griseri V. Polyimide used in space applications. In: Diaham S, editor. Polyimide for Electronic and Electrical Engineering Applications. London, UK: IntechOpen; 2020. pp. 1–9.
11. Rich FJ, Reasoner DL, Burke WJ. Plasma sheet at lunar distance: characteristics and interactions with the lunar surface. J Geophys Res. 1973; 78 (34): 8097–8112.
12. Manka RH. Plasma and potential at the lunar surface. In: Photon and Particle Interactions with Surfaces in Space: Proceedings of the 6th Eslab Symposium, Noordwijk, Netherlands, September 26–29, 1972. Dordrecht, Netherlands: Springer Netherlands; 1973. pp. 347–361.
13. Freeman JW, Ibrahim M. Lunar electric fields, surface potential and associated plasma sheaths. In: Lunar Science Institute, Conference on Interactions of the Interplanetary Plasma with the Modern and Ancient Moon, Lake Geneva, WI, USA, September 30–October 4, 1974. The Moon . 1975; 14: 103–114.
14. Halekas JS, Bale SD, Mitchell DL, Lin RP. Electrons and magnetic fields in the lunar plasma wake. J Geophys Res Space Phys. 2005; 110: A07222 .
15. Halekas JS, Lin RP, Mitchell DL. Large negative lunar surface potentials in sunlight and shadow. Geophys Res Lett. 2005; 32 (9): L09102.
16. Stubbs TJ, Halekas JS, Farrell WM, Vondrak RR. Lunar surface charging: a global perspective using Lunar Prospector data. Dust Planetary Syst. 2007; 643: 181–184.
17. Halekas JS, Delory GT, Brain DA, Lin RP, Fillingim MO, Lee CO, Mewaldt RA, Stubbs TJ, Farrell WM, Hudson MK. Extreme lunar surface charging during solar energetic particle events. Geophys Res Lett. 2007; 34 (2): L02111.
18. Halekas JS, Delory GT, Lin RP, Stubbs TJ, Farrell WM. Lunar surface charging during solar energetic particle events: measurement and prediction. J Geophys Res Space Phys. 2009; 114: A05110.

19. Farrell WM, Halekas JS, Killen RM, Delory GT, Gross N, Bleacher LV, Krauss-Varben D, Travnicek P, Hurley D, Stubbs TJ, Zimmerman MI. Solar-Storm/Lunar Atmosphere Model (SSLAM): an overview of the effort and description of the driving storm environment. J Geophys Res Planets. 2012; 117: E00K04.
20. Stubbs TJ, Farrell WM, Halekas JS, Burchill JK, Collier MR, Zimmerman MI, Vondrak RR, Delory GT, Pfaff RF. Dependence of lunar surface charging on solar wind plasma conditions and solar irradiation. Planetary Space Sci. 2014; 90: 10–27.
21. Breneman AW, Wygant JR, Tian S, Cattell CA, Thaller SA, Goetz K, Tyler E, Colpitts C, Dai L, Kersten K, Bonnell JW. The Van Allen Probes electric field and waves instrument: science results, measurements, and access to data. Space Sci Rev. 2022; 218 (8): 69.
22. Fennell JF, Roeder JL, Berg GA, Elsen RK. HEO satellite frame and differential charging and SCATHA low-level frame charging. IEEE Trans Plasma Sci. 2008; 36 (5): 2271–2279.
23. Leach RD. Failures and Anomalies Attributed to Spacecraft Charging. Huntsville, AL, USA: National Aeronautics and Space Administration, Marshall Space Flight Center; 1995.
24. Huang Z, Wang J. Modeling lunar surface charging under space weather conditions derived from the Artemis and Omni data. IEEE Trans Plasma Sci. 2023; 51 (9): 2515–2521.
25. Alad RH, Shah H, Chakrabarty SB, Shah D. Effect of solar illumination on ESD for structure used in spacecraft. Prog Electromagn Res M. 2017; 55: 25–36.
26. Gibson WC. The Method of Moments in Electromagnetics. New York, NY, USA: Chapman & Hall/CRC Press; 2007. pp. 33–48, 255–269.
27. Das BN, Chakrabarty SB. Capacitance and charge distribution of two cylindrical conductors of finite length. IEE Proc Sci Measure Technol. 1997; 144 (6): 280–286.
28. Bai EW, Lonngren KE. On the capacitance of a cube. Computers Electric Eng. 2002; 28 (4): 317–321.
29. Cañas-Peñuelas CS, Catalan-Izquierdo S, Bueno-Barrachina JM, Cavallé-Sesé F. Unit cube capacitance calculation by means of finite element analysis. In: International Conference on Renewable Energies and Power Quality, Valencia, Spain, April 15–17, 2009.
30. Harrington RF. Field Computation by Moment Methods. Hoboken, NJ, USA: Wiley-IEEE Press; 1993.
31. Alad RH, Chakrabarty SB. Capacitance and surface charge distribution computations for a satellite modeled as a rectangular cuboid and two plates. J Electrostatics. 2013; 71 (6): 1005–1010.
32. Das BN, Chakrabarty SB. Evaluation of capacitance and charge distribution of cylinder of finite length with top and bottom cover plates. Indian J Radio Space Phys. 1997; 26: 112–115.
33. Adams AT. Electromagnetics for Engineers. New York, NY, USA: Ronald Press; 1972. pp. 65–126, 166–220.
34. Kim CY. A numerical solution for the round disk capacitor by using annular patch subdomains. Prog Electromagn Res B. 2008; 8: 179–194.